A mechanism for oscillatory instability in viscoelastic cross-slot flow

LI XI AND MICHAEL D. GRAHAM†

Department of Chemical and Biological Engineering, University of Wisconsin-Madison,
Madison, WI 53706-1691, USA

Interior stagnation-point flows of viscoelastic liquids arise in a wide variety of applications including extensional viscometry, polymer processing and microfluidics. Experimentally, these flows have long been known to exhibit instabilities, but the mechanisms underlying them have not previously been elucidated. We computationally demonstrate the existence of a supercritical oscillatory instability of low-Reynolds-number viscoelastic flow in a two-dimensional cross-slot geometry. The fluctuations are closely associated with the 'birefringent strand' of highly stretched polymer chains associated with the outflow from the stagnation point at high Weissenberg number. Additionally, we describe the mechanism of instability, which arises from the coupling of flow with extensional stresses and their steep gradients in the stagnation-point region.

1. Introduction

While Newtonian flows become unstable only at high Reynolds number *Re*, when the inertial terms in momentum balance dominate, flows of viscoelastic fluids such as polymer solutions and melts are known to have interesting instabilities and nonlinear dynamical behaviours even at extremely low *Re*. These 'purely elastic' instabilities arise in rheometry of complex fluids as well as in many applications (Larson 1992; Shaqfeh 1996). Recent studies of viscoelastic flows in microfluidic devices broaden the scope of these nonlinear dynamical problems of viscoelastic flows (Squires & Quake 2005). The small length scales in microfluidic devices enable large shear rates, and thus high *Wi* (Weissenberg number, $Wi \equiv \lambda \dot{\gamma}$, where λ is a characteristic time scale of the fluid and $\dot{\gamma}$ is a characteristic shear rate of the flow), at very low *Re*. Instabilities are not always undesirable, especially when the accompanying flow modification is controllable and can thus be used in the design and operation of microfluidic devices. Specifically, instabilities have been found and flow-controlling logic elements have been designed in a series of microfluidic geometries, e.g. flow rectifier with anisotropic resistance (Groisman & Quake 2004), flip–flop memory (Groisman, Enzelberger & Quake 2003) and nonlinear flow resistance (Groisman *et al.* 2003). Another prospective application of these instabilities is to the enhancement of mixing at lab-on-a-chip length scales (Groisman & Steinberg 2001), where turbulent mixing is absent owing to small length scales and an alternative is required.

The best understood of these instabilities are those that occur in viscometric flows with curved streamlines: e.g. flows in Taylor–Couette (Muller, Shaqfeh & Larson 1989), Taylor–Dean (Joo & Shaqfeh 1994), cone-and-plate (Magda & Larson 1988)

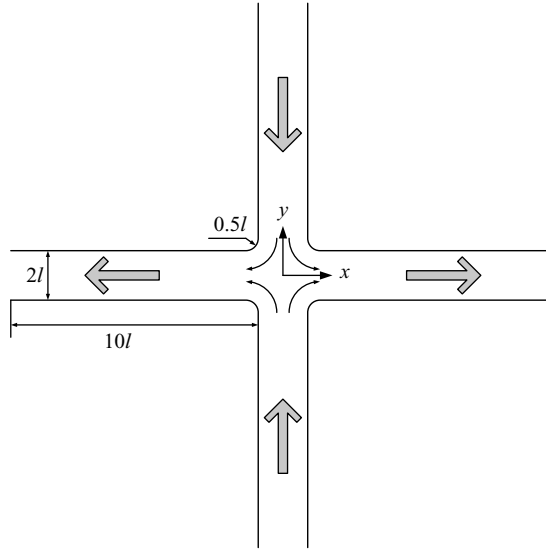† Email address for correspondence: graham@engr.wisc.edu

FIGURE 1. Schematic of the cross-slot flow geometry.

and parallel-plates (Groisman & Steinberg 2000; Magda & Larson 1988) flow geometries. In these geometries, the primary source of instability is the coupling of normal stresses with streamline curvature (i.e. the presence of 'hoop stresses'), leading to radial compressive forces that can drive instabilities (Magda & Larson 1988; Muller *et al.* 1989; Larson, Muller & Shaqfeh 1990; Joo & Shaqfeh 1994; Pakdel & McKinley 1996; Shaqfeh 1996; Graham 1998). Similar mechanisms drive instabilities in viscoelastic free-surface flows (Spiegelberg & McKinley 1996; Graham 2003).

Attention in this paper focuses on a different class of flows, whose instabilities are not well-understood – stagnation-point flows, such as those generated with opposed-jet (Chow *et al.* 1988; Müller, Odell & Keller 1988), cross-slot (Arratia *et al.* 2006), two-roll mill (Ng & Leal 1993) and four-roll mill (Ng & Leal 1993; Broadbent, Pountney & Walters 1978) devices. Figure 1 shows a schematic of a cross-slot geometry. A characteristic phenomenon in these stagnation-point flows is the formation of a narrow region of fluid with high polymer stress extending downstream from the stagnation point. This region can be observed in optical experiments as a bright birefringent 'strand' with the rest of the fluid dark (Harlen, Rallison & Chilcott 1990). Keller and coworkers (Chow *et al.* 1988; Müller *et al.* 1988) reported instabilities in stagnation-point flows of semi-dilute polymer solutions generated by an axisymmetric opposed-jet device. Specifically, for a fixed polymer species and concentration, upon a critical extension rate (or critical Wi) polymer chains become stretched by flow near the stagnation point and a sharp uniform birefringent stand forms. The width of this birefringent strand increases with increasing Wi until a stability limit is reached, beyond which the birefringent strand becomes destabilized, and changes in its morphology are observed. At higher Wi, the flow pattern and birefringent strand become time-dependent. Tracer and particle-tracking experiments of stagnation point flow in a micro-fabricated cross-slot geometry by Arratia *et al.* (2006) show instabilities of dilute polymer solution at low $Re\,(< 10^{-2})$. In their experiments, fluid from one of the two incoming channels is dyed and a sharp and flat interface between dyed and undyed fluids is observed at low Wi.

Upon an onset value of Wi, this flow pattern loses its stability: spatial symmetry is broken, but the flow remains steady. The interface becomes distorted in such a way that more than half of the dyed fluid goes to one of the outgoing channels while more undyed fluid travels through the other. At even higher Wi, the flow becomes time-dependent and the direction of asymmetry flips between two outgoing channels with time. Particle-tracking images in the time-dependent flow pattern indicate the existence of vortical structures around the stagnation point.

Another class of stagnation-point flows is associated with liquid–solid or liquid–gas interfaces, such as flows passing submerged solid obstacles, around moving bubbles or toward a free surface. For example, McKinley, Armstrong & Brown (1993) reported three-dimensional steady cellular disturbances in the wake of a cylinder submerged in a viscoelastic fluid. Around a falling sphere in viscoelastic fluids, the fore-and-aft symmetry of the velocity field is broken and the velocity perturbation in the wake can be away from the sphere, toward the sphere or a combination of the two, depending on the polymer solution (Hassager 1979; Bisgaard & Hassager 1982; Bisgaard 1983).

Remmelgas, Singh & Leal (1999) computationally studied the stagnation-point flow in a cross-slot geometry with two different FENE (finitely extensible nonlinear elastic) dumbbell models. Using the two models, they studied the effects of configuration-dependent friction coefficient on polymer relaxation and the shape of the birefringent strand. Their simulation approach was restricted to relatively low $Wi(\sim O(1))$ with symmetry imposed on the centrelines of all channels. Harlen (2002) conducted simulations of a sedimenting sphere in a viscoelastic fluid to explore the wake behaviours. He explains the experimental observations of both negative (velocity perturbation away from the sphere) and extended (velocity perturbation toward the sphere) wakes in terms of combined effects of the stretched polymer in the birefringent strand following the stagnation point behind the sphere and the recoil outside of the strand. Neither of these analyses directly addressed instabilities of these flows. In Poole, Alves & Oliveira (2007), a stationary symmetry-breaking instability in the cross-slot geometry has been predicted by conducting simulations using the upper-convected Maxwell model. This instability is similar to the first steady symmetry-breaking instability in the experiments of Arratia *et al.* (2006). However, the question as to why the flow field becomes time-dependent in different geometries involving stagnation points still needs to be addressed.

Various approximate approaches have been taken in the past to obtain an understanding of the instabilities observed in experiments. Harris & Rallison (1993, 1994) investigated the instabilities of the birefringent strand downstream of a free isolated stagnation point through a simplified approach, in which polymer molecules are modelled as linear-locked dumbbells, which are fully stretched within a thin strand lying along the centreline. Polymer molecules contribute a normal stress proportional to the extension rate only when they are fully stretched (i.e. in the strand); otherwise, the flow is treated as Newtonian. The lubrication approximation is applied for the Newtonian region and the effects of the birefringent strand are coupled into the problem through point forces along the strand. Two instabilities are reported. At low $Wi(\approx 1.2-1.7)$, a varicose disturbance is linearly unstable, in which the width of the birefringent strand oscillates without breaking the symmetry of the flow pattern. At higher Wi, another instability is observed in which symmetry with respect to the extension axis breaks and the birefringent strand becomes sinuous in shape and oscillatory with time, with zero displacement at the stagnation point and increasing magnitude of displacement downstream from it. Symmetry with respect to

the inflow axis is always imposed. The mechanism of these instabilities is explained: perturbations in the shape or position of the birefringent strand affect the stretching of incoming polymer molecules such that they enhance the perturbation after they become fully stretched and merge into the strand. This mechanism is close to the one that we present later in this paper with regard to the importance of flow kinematics and the extensional stress. However, in their linear stability analysis with which the instability mechanism is investigated, the spatial dependence of the birefringent strand in the outflow direction is neglected. Therefore, although this factor is included in their numerical simulation, it is not taken into consideration in their explanation of the instability. As will be shown later, according to our simulations, this spatial dependence of the birefringent strand plays an important role.

In this paper, we present numerical simulation results of viscoelastic stagnation point flow in a two-dimensional cross-slot geometry. With increasing Wi, we observe the formation and elongation of the birefringent strand across the stagnation point. At high Wi, we find the occurrence of an oscillatory instability. These results resemble the experimental observations of oscillatory birefringent width by Müller *et al.* (1988) and the varicose instability predicted by Harris & Rallison (1994). By analysing the perturbations in both velocity and stress fields, a novel instability mechanism based on normal stress effects and flow kinematics is identified.

2. Formulation and methods

We consider a fourfold symmetric planar cross-slot geometry, as shown in figure 1. Flow enters from top and bottom and leaves from left and right. For laminar Newtonian flow, two incoming streams meet at the intersection of the cross and each of them splits evenly and goes into both outgoing channels, generating a stagnation point at the origin near which an extensional flow exists. We use round corners at the intersections of channel walls in order to avoid enormous stress gradients at the corners, which cause numerical difficulties.

The momentum and mass balances are:

$$Re\left(\frac{\partial \boldsymbol{u}}{\partial t} + \boldsymbol{u}\cdot\nabla\boldsymbol{u}\right) = -\nabla p + \beta\nabla^2\boldsymbol{u} + (1-\beta)\frac{2}{Wi}(\nabla\cdot\boldsymbol{\tau}_p), \qquad (2.1)$$

$$\nabla\cdot\boldsymbol{u} = 0. \qquad (2.2)$$

Parameters in (2.1) and (2.2) are defined as: $Re \equiv \rho U l / (\eta_s + \eta_p)$, $Wi \equiv 2\lambda U/l$ and $\beta \equiv \eta_s / (\eta_s + \eta_p)$, where ρ is the fluid density, for a dilute polymer solution we assume it to be the same as the solvent density; η_s is the solvent viscosity and η_p is the polymer contribution to the shear viscosity at zero shear rate and U and l are characteristic velocity and length scales of the flow. Here, l is chosen to be the half-channel width and the definition of U is based on the pressure drop applied between the entrances and exits of the channel. Specifically, U is defined to be the centreline velocity of a Newtonian plane Poiseuille flow under the same pressure drop in a straight channel with length $20l$, which is comparable to the lengths of streamlines in the present geometry. According to this definition, the non-dimensional pressure drop in our simulation is fixed at 40 and the centreline Newtonian velocity in cross-slot geometry is typically slightly lower than 1 since the extensional flow near the stagnation point has a higher resistance than that in a straight channel. The polymer contribution to the stress tensor is denoted $\boldsymbol{\tau}_p$ and is calculated with the

FENE-P constitutive equation (Bird *et al.* 1987):

$$\frac{\boldsymbol{\alpha}}{1 - \mathrm{tr}(\boldsymbol{\alpha})/b} + \frac{Wi}{2}\left(\frac{\partial\boldsymbol{\alpha}}{\partial t} + \boldsymbol{u}\cdot\nabla\boldsymbol{\alpha} - \boldsymbol{\alpha}\cdot\nabla\boldsymbol{u} - (\boldsymbol{\alpha}\cdot\nabla\boldsymbol{u})^T\right) = \left(\frac{b}{b+2}\right)\boldsymbol{\delta}, \quad (2.3)$$

$$\boldsymbol{\tau}_p = \frac{b+5}{b}\left(\frac{\boldsymbol{\alpha}}{1 - \mathrm{tr}(\boldsymbol{\alpha})/b} - \left(1 - \frac{2}{b+2}\right)\boldsymbol{\delta}\right). \quad (2.4)$$

In (2.3) and (2.4), polymer chains are modelled as FENE dumbbells (two beads connected by a finitely-extensible-nonlinear-elastic spring). Here, $\boldsymbol{\alpha} \equiv \langle\boldsymbol{QQ}\rangle$ is the conformation tensor of the dumbbells where $\boldsymbol{Q}$ is the end-to-end vector of the dumbbells and $\langle\cdot\rangle$ represents an ensemble average. The parameter b determines the maximum extension of the dumbbells: i.e. the upper limit of $\mathrm{tr}(\boldsymbol{\alpha})$.

At the entrances and exits of the flow geometry, normal flow boundary conditions are applied: i.e. $\boldsymbol{t}\cdot\boldsymbol{u} = 0$ where $\boldsymbol{t}$ is the unit vector tangential to the boundary. Pressure is set to be 40 at entrances and 0 at exits. No-slip boundary conditions are applied at all other boundaries. Boundary conditions for stress are only required at the entrances, where the profile of $\boldsymbol{\alpha}$ is set to be the same as that for a fully developed pressure-driven flow in a straight channel with the same Wi. Unless otherwise noted, several parameters are fixed for most of the results we report here: $Re = 0.1$, $\beta = 0.95$ and $b = 1000$, which means we focus on dilute solutions of long-chain polymers at low Reynolds number.

The discrete elastic stress splitting (DEVSS) formulation (Baaijens *et al.* 1997; Baaijens 1998) is applied in our simulation: i.e. a new variable $\boldsymbol{\Lambda}$ is introduced as the rate of strain and a new equation is added into the equation system:

$$\boldsymbol{\Lambda} = \nabla\boldsymbol{u} + \nabla\boldsymbol{u}^T. \quad (2.5)$$

A numerical stabilization term $\gamma\nabla\cdot(\nabla\boldsymbol{u} + \nabla\boldsymbol{u}^T - \boldsymbol{\Lambda})$ is added to the right-hand side of the momentum balance (equation (2.1)) and it is worth pointing out that this term is only non-trivial in the discretized formulation and does not change the physical problem. In this term, γ is an adjustable parameter and $\gamma = 1.0$ is used in our simulations. The velocity field $\boldsymbol{u}$ is interpolated with quadratic elements while pressure p, polymer conformation tensor $\boldsymbol{\alpha}$ and rate of strain $\boldsymbol{\Lambda}$ are interpolated with linear elements. Consistent with Baaijens's (1998) conclusion, DEVSS greatly increases the upper limit of Wi achievable in our simulations. Quadrilateral elements are used for all variables. Our experience shows that quadrilateral elements have great advantages over triangular ones, yielding much better spatial smoothness in the stress field at comparable degrees of freedom to be solved. Another merit of quadrilateral elements is the capability of manual control over mesh grids. This is extremely important when certain restrictions, such as symmetry, are required. In our simulation, finer meshes are used within and around the intersection region of the geometry and the mesh is required to be symmetric with respect to both axes. Within a horizontal band $(-0.2 < y < 0.2)$ across the stagnation point, very fine meshes are generated to capture the sharp stress gradient along the birefringent strand. The streamline upwind/Petrov–Galerkin method (SUPG) (Brooks & Hughes 1982) is applied in (2.3) by replacing the usual Galerkin weighting function w with $w + \delta h\boldsymbol{u}\cdot\nabla w/\|\boldsymbol{u}\|$, where h is the geometric average of the local mesh length scales and δ is an adjustable parameter, set to $\delta = 0.3$ in our simulations. This formulation is implemented using the commercially available *COMSOL Multiphysics* software.
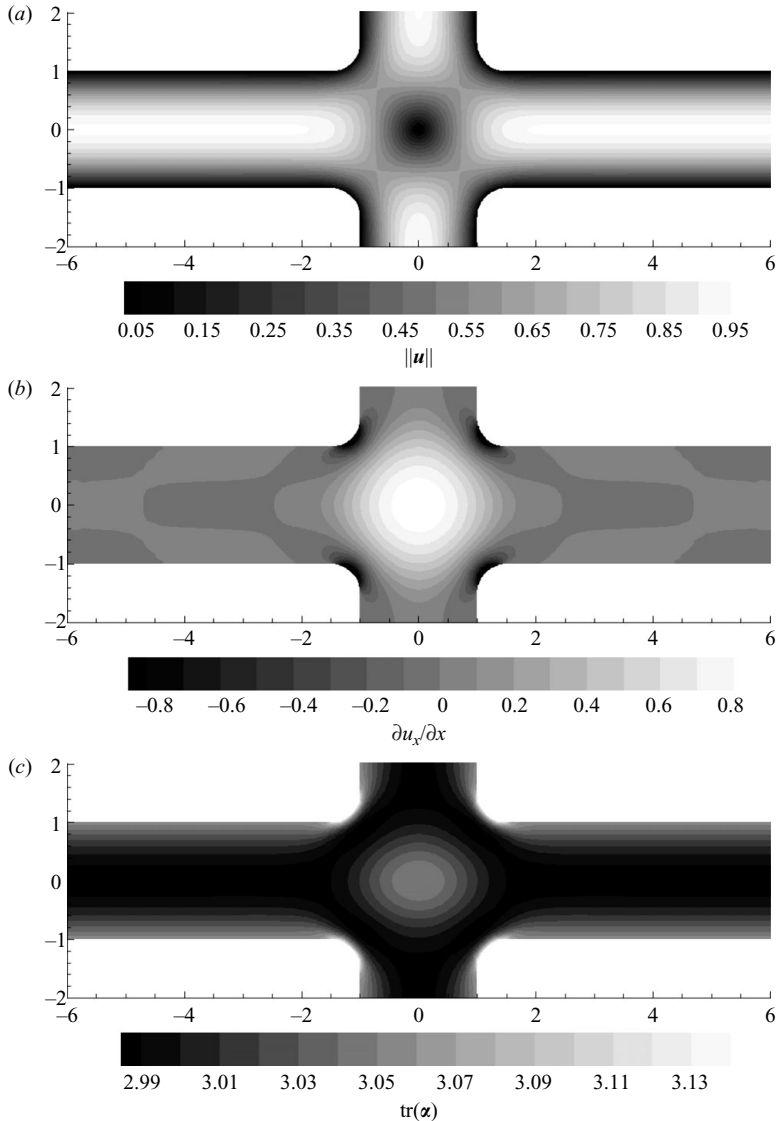
FIGURE 2. Contour plots of steady-state solution: $Wi = 0.2$ (only the central part of the flow domain is shown).

3. Results and discussion

3.1. *Steady states*

Steady-state solutions are found for all Wi investigated ($0.2 < Wi < 100$) in our study. For $Wi \leqslant 60$, steady states are found by time integration and for those with larger Wi, Newton iteration (parameter continuation) is used because of possible loss of stability, as we describe below. At low Wi, the velocity field is virtually unaffected by the polymer molecules. Velocity contours at $Wi = 0.2$ are plotted in figure 2(a); for clarity, only part of the channel is shown. A stagnation point is found at the centre of the domain ($(0, 0)$). In both incoming and outgoing channels, the flow is almost the same as pressure-driven flow in a straight channel. No distinct difference can be
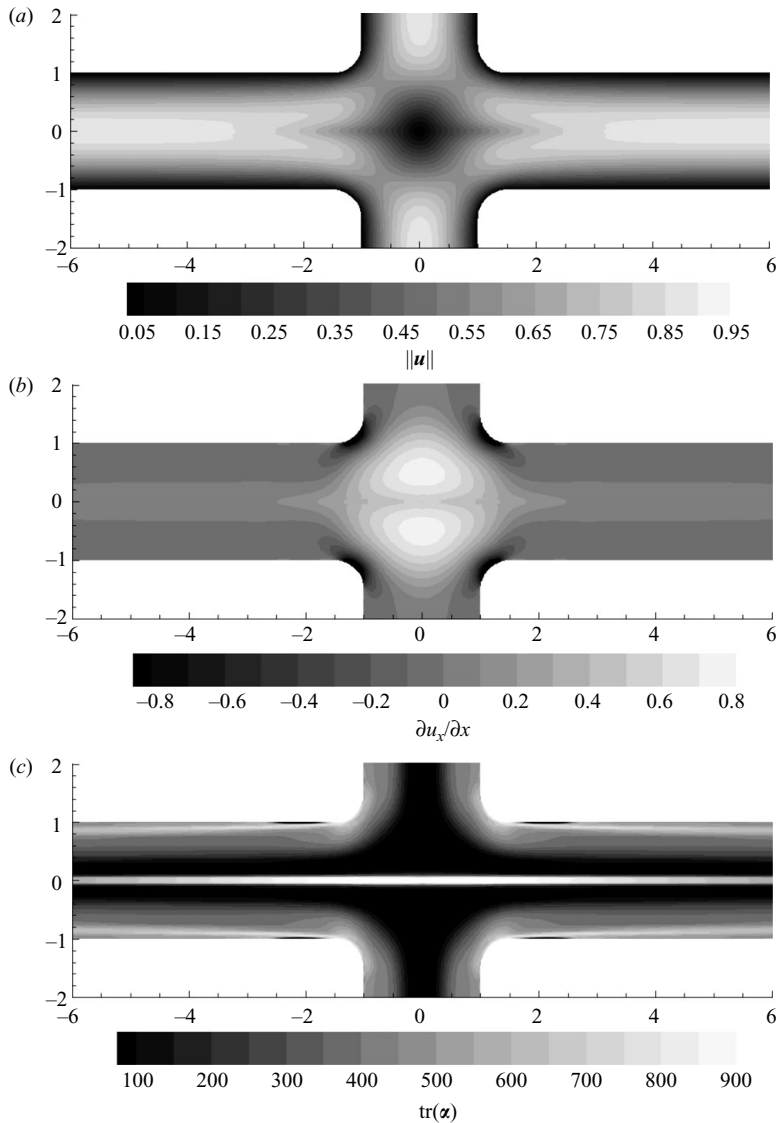
FIGURE 3. Contour plots of steady state solution: $Wi = 50$ (only the central part of the flow domain is shown).

observed for the incoming and outgoing directions in velocity field. figure 2(*b*) shows contours of extension rate at $Wi = 0.2$, in which a region dominated by extensional flow is found near the stagnation point. A high extension rate is also found near the corners owing to the no-slip walls. The magnitude of polymer stretching can be measured by the trace of its conformation tensor $tr(\alpha)$, and is plotted in figure 2(*c*). At low Wi, the extent to which polymers are deformed is barely noticeable, but it can be clearly seen that polymers are primarily stretched in either the extensional flow near the stagnation point and corners or the shear flows near the walls. At high Wi ($Wi = 50$, figure 3), the situation is very different. Polymers are strongly stretched by the extensional flow near the stagnation point and this stretching effect by extensional flow overwhelms that of the shear flow. A distinct band of highly stretched polymers
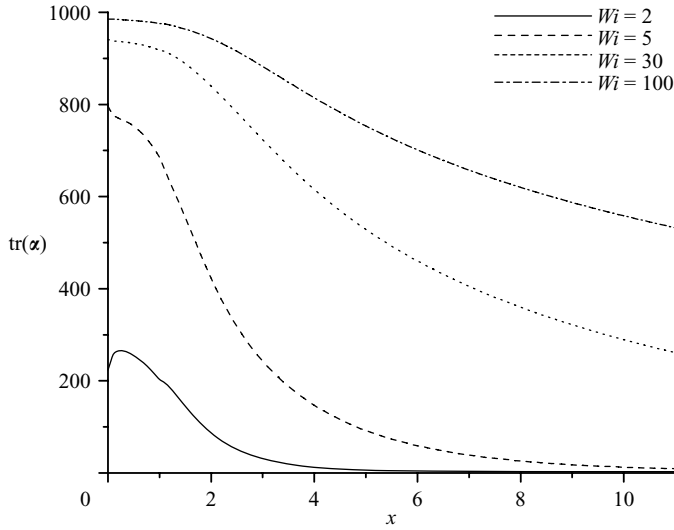
FIGURE 4. Profile of $\mathrm{tr}(\boldsymbol{\alpha})$ along $y = 0$.
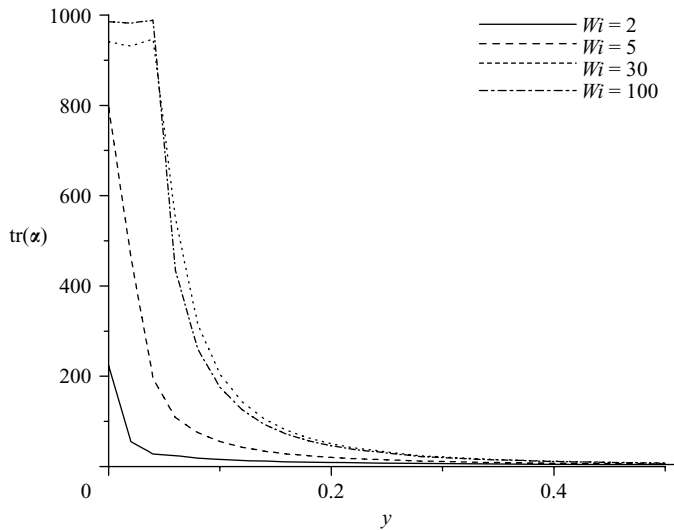
FIGURE 5. Profile of $\mathrm{tr}(\boldsymbol{\alpha})$ along $x = 0$ in the region very near the stagnation point.

(the birefringent strand) forms (figure 3c). Since the polymer relaxation time in this case is larger than the flow convection time from the stagnation point to the exits, this birefringent strand extends the whole length of the simulation domain. The resulting high polymer stress significantly affects the velocity field (figure 3a). Regions with reduced velocity extend much farther away in the downstream directions of the stagnation point than in the low Wi case, especially along the x-axis, where high polymer stress dominates. Correspondingly, a reduction in the extension rate near the stagnation point is observed, most noticeably along the birefringent strand (figure 3b).

Figures 4 and 5 show profiles at various values of Wi of $\mathrm{tr}(\boldsymbol{\alpha})$ along the outflow (x-axis) and inflow (y-axis) directions of this stagnation point (note the difference in scales in the two plots). For increasing Wi, the length of the region with highly stretched
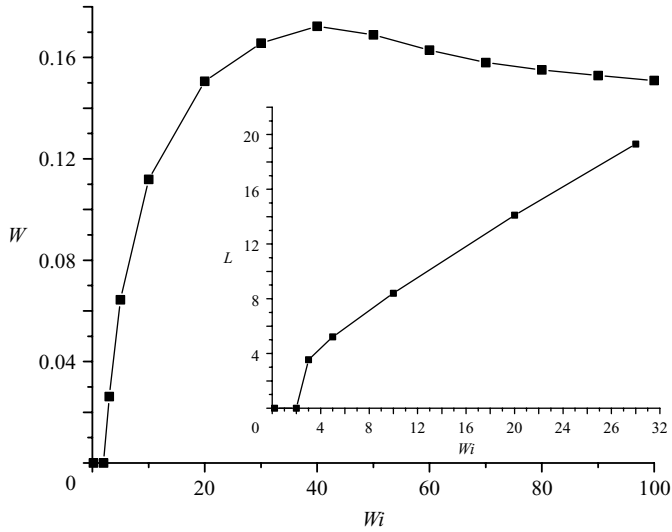
FIGURE 6. Birefringent strand width W; inset: Birefringent strand length L ($\text{tr}(\boldsymbol{\alpha}) > 300$ is considered as the observable birefringence region).

polymer keeps increasing owing to the increased relative relaxation time (figure 4). In high Wi cases ($Wi = 30$ and $Wi = 100$), polymers are not fully relaxed even when they reach the exit of the simulation domain. The cross-sectional view of the $\text{tr}(\boldsymbol{\alpha})$ profile along the y-axis (figure 5) shows interesting non-monotonic behaviours. Although the height of the profile ($\text{tr}(\boldsymbol{\alpha})_{max}$) keeps increasing on increasing Wi, the width of the $Wi = 100$ case is smaller than that of $Wi = 30$, resulting in a steeper transition section between low and high stretching regions. If we arbitrarily define $\text{tr}(\boldsymbol{\alpha}) > 300$ as the observable birefringence region, the width W and the length L of the birefringent strand (measured on the inflow and outflow axes, respectively) can be plotted as functions of Wi, as in figure 6 (values of L for $Wi > 30$ are not shown since they exceed the length of the simulation domain). A clear non-monotonic trend is observed in the plot of birefringence width, where W increases sharply at relatively low Wi, and peaks around $Wi = 40$. After that, W decreases mildly, but consistently, with further higher Wi. This non-monotonic trend is consistent with experimental observations of birefringence in opposed-jet devices (Müller *et al.* 1988).

Similarly, a non-monotonicity is also found in the change of velocity field with Wi. Shown in figure 7 is the value of extension rate, averaged within a box around the stagnation point ($-0.1 < x < 0.1, -0.1 < y < 0.1$), as a function of Wi. As Wi increases, the extension rate decreases at low Wi, but increases at high Wi, with a minimum found around $Wi = 40$. Besides, most of experimental results are presented in terms of Deborah number (De), defined as the product of the polymer relaxation time and an estimate of the extension rate near the stagnation point. Noticing that the average (non-dimensionlized) extension rate changes within a very narrow range (around 0.55–0.6), a conversion $De = 0.3Wi$ can be adopted for comparison of our results with experimental ones.

Some understanding of this non-monotonicity can be gained by looking at figure 4. Here it can be seen that for $Wi \lesssim 30$, the birefringent strand is not yet 'fully developed' in the sense that the polymer stretching is not yet saturating near full extension. Thus, the evolution of the velocity field in this regime of Wi reflects the significant changes
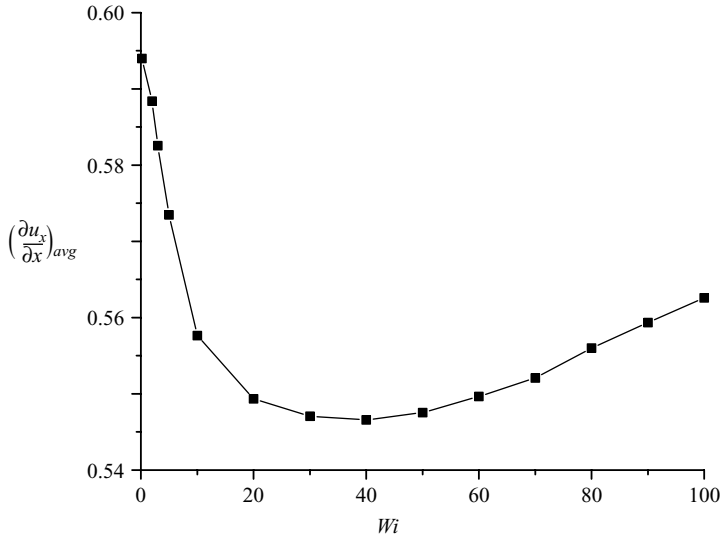
L. Xi and M. D. Graham

FIGURE 7. Average extension rate $(\partial u_x/\partial x)_{avg}$ (averages taken in the domain
$-0.1 < x < 0.1, -0.1 < y < 0.1$).

that occur in the stress field in this regime. At higher Wi, however, the polymer stress field in the strand is saturating, and thus not changing significantly. Furthermore, at these high Weissenberg numbers, the relaxation of stress downstream of the stagnation point diminishes, decreasing the gradient $\partial\tau_{xx}/\partial x$ and thus decreasing the effect of viscoelasticity on the flow near the stagnation point.

3.2. *Periodic orbits*

We turn now to the stability of the steady states that have just been described. Rather than attempting to compute the eigenspectra of the linearization of the problem, an exceedingly demanding task, we examine stability by direct time integration of perturbed steady states. The perturbations take the form of slightly asymmetric pressure profiles at the two entrances (0.1 % maximum deviation from the steady-state value) that are applied for one time unit, then released. As an example, figure 8 shows a two-dimensional projection of the trajectory of the system evolution over time at $Wi = 66$. Here, the velocity magnitude at a point near the stagnation point $((0.5, 0))$ is plotted against the birefringent strand width W measured on the inflow axis. The system starts at the steady-state with $W = 0.1593$ and $\|\boldsymbol{u}\|_{(0.5,0)} = 0.2687$ and spirals outward with time after the perturbation. Eventually, the trajectory merges into a cycle (the outer dark cycle in the figure 8). This clearly identifies the existence of a stable periodic orbit. Note the anticorrelation between $\|\boldsymbol{u}\|$ and W, i.e. when the flow speeds up near the stagnation point, the strand thins and vice versa. Although a finite asymmetric perturbation has been introduced in the simulation results presented here, it is worth mentioning that in order to trigger the instability, the initial perturbation does not have to be in this particular form, nor does it have a finite threshold. We have tested another form of perturbation in which we add zero-mean random noises of different orders-of-magnitude onto the initial steady-state solutions and the instability can always be observed.

Figure 9 shows the root-mean-square deviations over one period of W from its steady-state values, normalized by the corresponding steady-state values $W_{s.s.}$, as a function of Wi for all the cases where we found periodic orbits. Time integrations
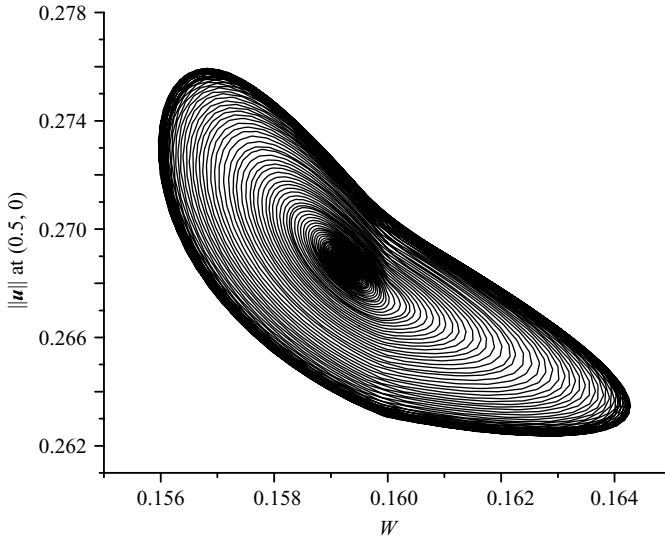
FIGURE 8. Two-dimensional projection of the dynamic trajectory from the steady state to the periodic orbit at $Wi = 66$: $\|\boldsymbol{u}\| = \sqrt{u_x^2 + u_y^2}$ at $(0.5, 0)$ *vs.* W.
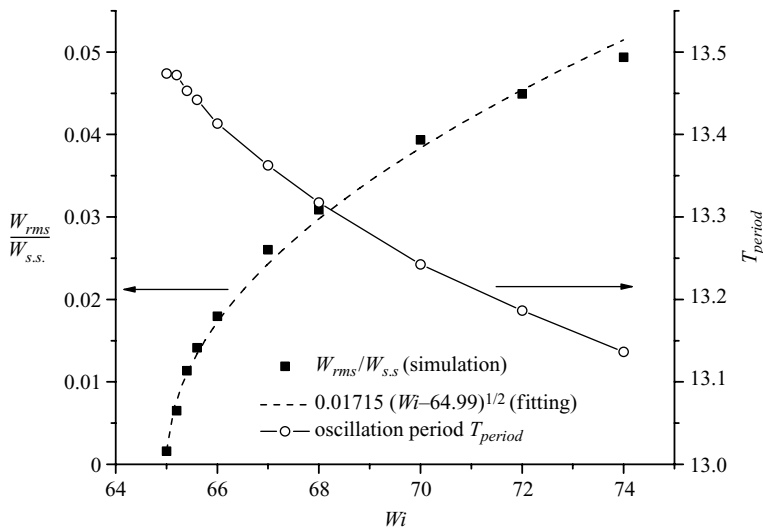

FIGURE 9. Left-hand axis: Root mean square deviations of the birefringent strand width W at periodic orbits, normalized by steady-state values; right-hand axis: oscillation periods.

for $Wi > 74$ did not converge owing to the enormous stress gradient around the corners of the no-slip walls and the consequent numerical oscillations downstream. Data points for W_{rms} computed from our simulations are fitted with a function of the form $a(Wi - Wi_c)^c$, with c fixed at $1/2$. Very good agreement is found for our simulation data with the $1/2$ power law, characteristic of a supercritical Hopf bifurcation (Guckenheimer & Holmes 1983). The critical Weissenberg number Wi_c is identified as 64.99 by this fitting. Also shown in figure 9 are periods of oscillations, where a slight decrease with increasing Wi is found. This indicates that some time scale other than the polymer relaxation time sets the period of oscillations.

Simulations have also been conducted at other values of β and b. Within the dilute regime, Wi_c has a strong dependence on the polymer concentration ($\propto (1 - \beta)$) and the bifurcation occurs at much higher Wi for more dilute solutions. (In the Newtonian limit $\beta \to 1$, Wi_c must diverge.) For example, for $\beta = 0.96$, Wi_c lies between 80 and 82. Simulations for lower β, i.e. higher concentration, are not feasible at this point owing to numerical instabilities. For b values not very far way from 1000, changing the b parameter barely affects Wi_c. By changing the b parameter downward to 900, Wi_c is almost unchanged. However, for further smaller b values, the dependence is stronger and Wi_c increases with decreasing b.

As mentioned earlier, time-dependent instabilities have been observed in viscoelastic stagnation-point flows in both opposed-jet and cross-slot geometries. In particular, the birefringent stability found by Müller *et al.* (1988) is very similar to the one reported in this paper. In their optical experiments with semi-dilute aPS solutions, the width of the birefringent strand oscillates rapidly between two values in a certain range of extension rate. Compared with their experiments, as well as the asymptotic model of Harris & Rallison (1994), our simulation predicts a higher critical Wi. This could be as least partially attributed to the low concentration we are looking at. In the cross-slot geometry, time-dependent oscillations are found for $De \geqslant 12.5$ (Arratia *et al.* 2006), which is of the same order-of-magnitude as what we have observed ($De_c \approx 0.3Wi_c = 19.5$). Although symmetry is not imposed in our simulations, we do not observe any symmetry-breaking instability, which according to the experiments should occur at a much lower De. This might be related to the constant-pressure constraints we applied on entrances and exits. In both the experiments (Arratia *et al.* 2006) and simulations (Poole *et al.* 2007) where asymmetry is observed, there are no restrictions on the pressure at the boundaries and constant-flow-rate constraints are applied instead.

3.3. *Instability mechanism*

We turn now to the spatiotemporal structure of the instability and its underlying physical mechanism. We will denote the deviations in velocity, pressure and stress with primes, while steady-state values will be denoted with a superscript 's':

$$\boldsymbol{u} = \boldsymbol{u}^s + \boldsymbol{u}', \tag{3.1}$$

$$p = p^s + p', \tag{3.2}$$

$$\boldsymbol{\alpha} = \boldsymbol{\alpha}^s + \boldsymbol{\alpha}'. \tag{3.3}$$

Figures 10, 11 and 12 illustrate u'_x, u'_y and α'_{xx}, respectively, at intervals of 1/8 period, corresponding to the periodic orbit at a Weissenberg number close to the bifurcation point ($Wi = 66$). Time starts from an arbitrarily chosen snapshot on the periodic orbit and only a quarter of the region near the stagnation point is shown; behaviour in the rest of the domain can be inferred from the reflection symmetry across the axes.

At the beginning of the cycle (figure 10*a*), u'_x is positive in the region very close to the stagnation point while it is negative in most of the downstream region. As time goes on, this positive deviation near the stagnation point grows into a 'jet', a region of liquid moving downstream away from the stagnation point faster than the steady-state velocity, as shown in figures 10(*b*), 10(*c*) and 10(*d*). Correspondingly, by continuity, the inflow toward the stagnation point is also faster, as shown in figures 11(*a*)–11(*d*). Note that very near the stagnation point, deviations from steady state remain small. At the beginning of the second half of the cycle (figure 10*e*), the jet extends further downstream and grows to the full width of the channel. Meanwhile, in the region closer to the stagnation point, velocity deviations drop (figures 10*e*, 11*e*) and start
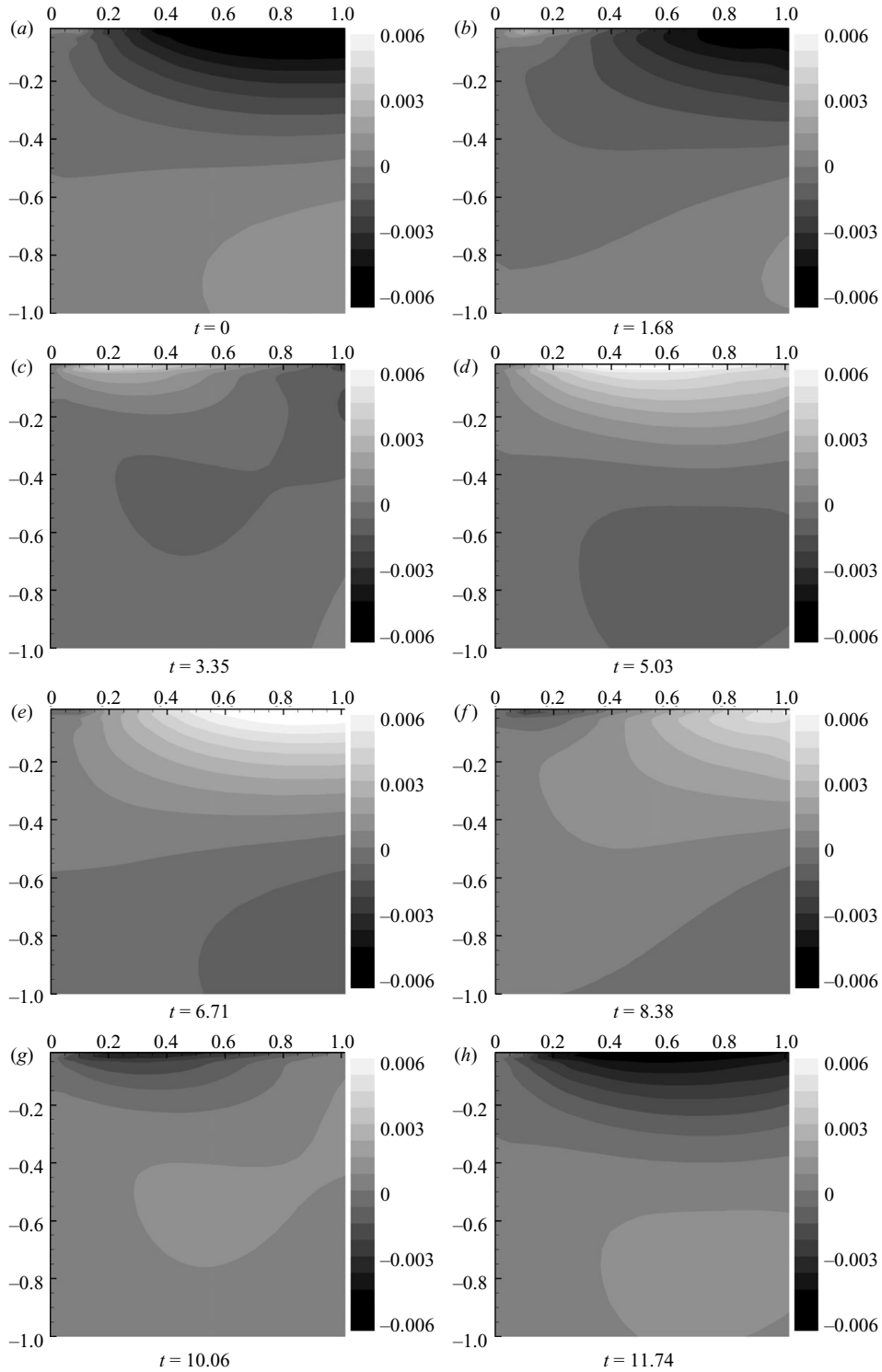
FIGURE 10. Perturbation of the x-component of velocity, u'_x with respect to steady state at the periodic orbit: $Wi = 66$. The region shown is $0 < x < 1$, $-1 < y < 0$; the stagnation point is at the top left-hand corner.

FIGURE 11. Perturbation of the y-component of velocity, u'_y with respect to steady state at the periodic orbit: $Wi = 66$. The region shown is $0 < x < 1$, $-1 < y < 0$; the stagnation point is at the top left-hand corner.

FIGURE 12. Perturbation of the *xx*-component of polymer conformation tensor, α'_{xx} with respect to steady state at the periodic orbit: $Wi = 66$. The region shown is $0 < x < 1$, $-1 < y < 0$; the stagnation point is at the top left-hand corner. The edge of the steady-state birefringent strand is the line $y \approx -0.05$.
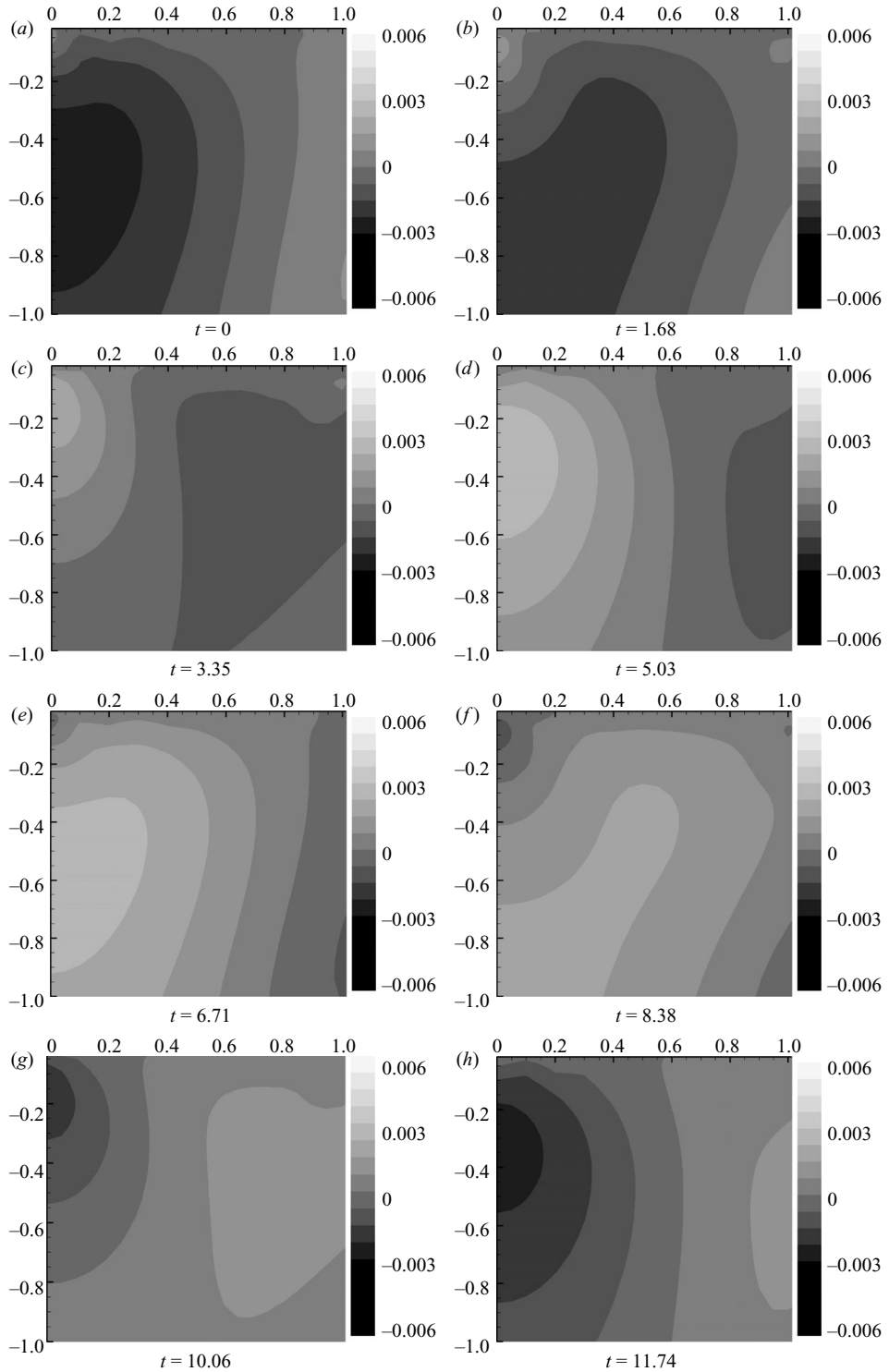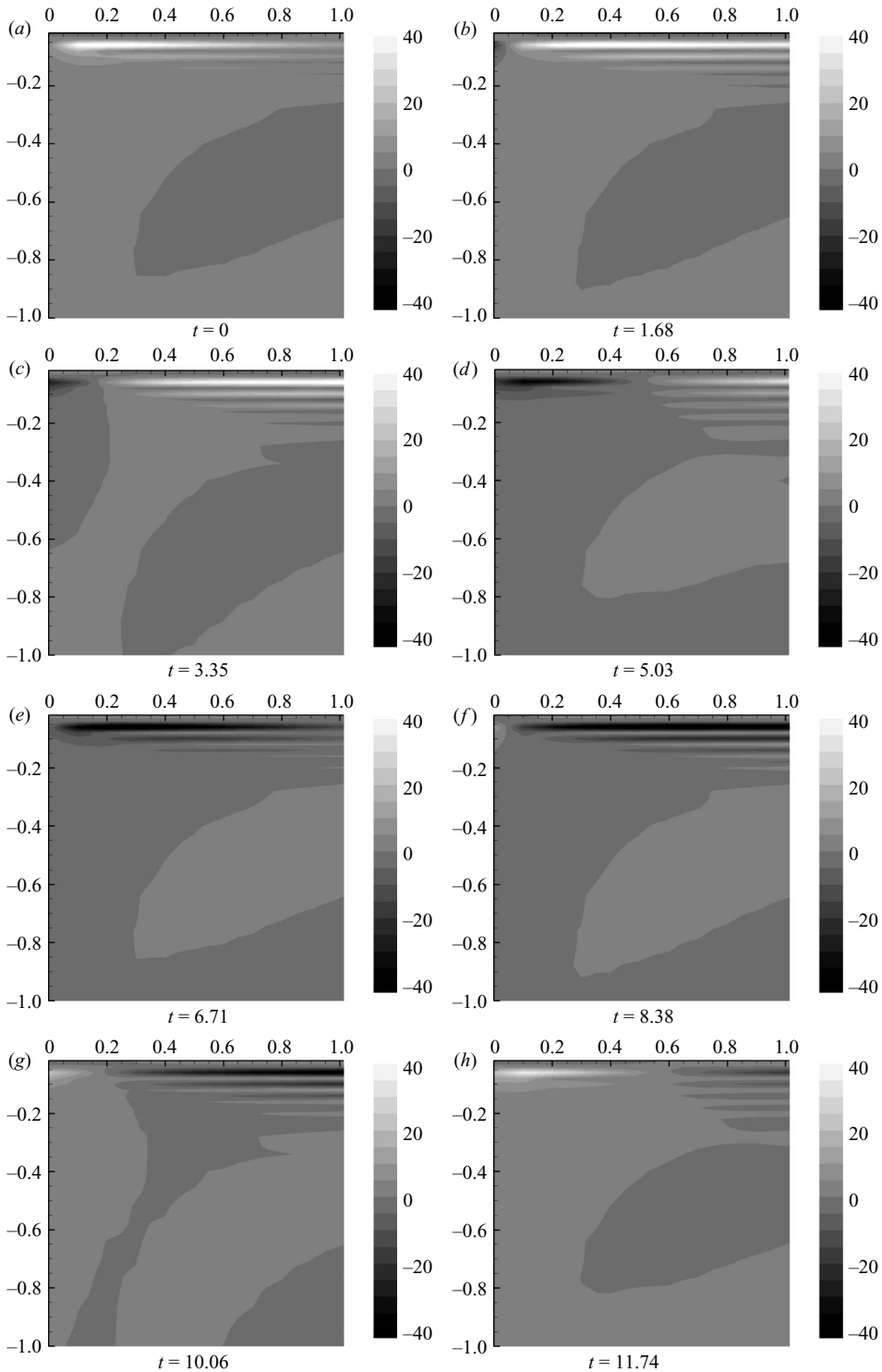
to change sign (figures 10*f*, 11*f*). Consequently, the growth of the jet ends and a 'wake', a region of fluid moving slower than the steady-state velocity, emerges from the stagnation point (figures 10*f*–*h* and 11*f*–*h*). Similarly, as the wake grow larger, velocity deviations near the stagnation point change signs and a new cycle starts (figures 10*a* and 11*a*).

The velocity deviations are closely related with those of the stress field (figure 12). Generally speaking, 'jets' are accompanied by negative α'_{xx} and thus thinning of the birefringent strand and 'wakes' are associated with the birefringent thickening. The largest deviations are found at the edges of the birefringent strand where $\partial \alpha^s_{xx}/\partial y$ is largest. Note that deviations in the stress field are always small along the centreline of the birefringent strand because there polymer molecules are almost fully stretched and the huge spring force is sufficient to resist any perturbations.

We can see the small spatial oscillations in the stress field deviations, characterized by alternating high and low stress stripes, along the outflow direction. These oscillations, apparently unphysical and centred around zero, also exist along the birefringence strand in steady-state solutions, though they are not easy to see from the contours in figure 3 (*c*) as they are overwhelmed by the high tr($\boldsymbol{\alpha}$) in the birefringent strand. Unfortunately, as shown by Renardy (2006) and Thomases & Shelley (2007), spatial non-smoothness is inevitable in numerical simulations of viscoelastic extensional flow upon certain *Wi* owing to the singularities in stress gradients. These singularities could not be fully resolved by any finite mesh size and this problem would always show up in numerical solutions of high *Wi* viscoelastic stagnation-point flows. However, we do not expect these oscillations to qualitatively affect our observations for a couple of reasons. First, non-smoothness has been observed in our simulation at *Wi* values much lower than the critical *Wi* of this instability. Secondly, observable non-smoothness is always found some distance away from the stagnation point in the downstream direction while the instability is dominated by the physics in the close vicinity of the stagnation point and, since FENE-P is a convective equation, we do not expect anything occurring downstream to affect upstream dynamics. Last, and most importantly, simulations with different meshes display different mesh-size-dependent stripes, while the nature of the instability remains virtually unchanged.

Insight into the mechanism of this instability can be gained by examining the linearized equation for α'_{xx}:

$$
\begin{aligned}
\frac{\partial \alpha'_{xx}}{\partial t} = {} & -\frac{2}{Wi}\frac{\alpha'_{xx}}{1 - \mathrm{tr}(\boldsymbol{\alpha}^s)/b} - \frac{2}{Wi}\frac{\alpha^s_{xx}\,\mathrm{tr}(\boldsymbol{\alpha}')}{b\,(1 - \mathrm{tr}(\boldsymbol{\alpha}^s)/b)^2} \\
& - u^s_x\frac{\partial \alpha'_{xx}}{\partial x} - u^s_y\frac{\partial \alpha'_{xx}}{\partial y} - u'_x\frac{\partial \alpha^s_{xx}}{\partial x} - u'_y\frac{\partial \alpha^s_{xx}}{\partial y} \\
& + 2\alpha^s_{xx}\frac{\partial u'_x}{\partial x} + 2\alpha^s_{xy}\frac{\partial u'_x}{\partial y} + 2\alpha'_{xx}\frac{\partial u^s_x}{\partial x} + 2\alpha'_{xy}\frac{\partial u^s_x}{\partial y}.
\end{aligned}
\tag{3.4}
$$

In the following analysis, terms on the right-hand side (RHS) of (3.4) are named 'RHS∗', where '∗' is determined by the order of appearance on the RHS. Terms and their physical meanings are summarized in table 1. To understand the mechanism of the instability, magnitudes of these terms at the point $(0, -0.05)$ are plotted as a function of time during roughly a period in figure 13(*b*). Terms RHS3, RHS5, RHS8 and RHS10 are zero by symmetry and not plotted. This position is at the edge of the birefringent strand and as shown in figure 12, it is also where significant deviations in the stress field are observed. Time-dependent oscillations at other places, including off the symmetry axis $x = 0$, have also been checked and nothing that would qualitatively

Term	Formula	Physical significance
RHS1	$-\dfrac{2}{Wi}\dfrac{\alpha'_{xx}}{1-\mathrm{tr}(\boldsymbol{\alpha}^{s})/b}$	Relaxation.
RHS2	$-\dfrac{2}{Wi}\dfrac{\alpha^{s}_{xx}\mathrm{tr}(\boldsymbol{\alpha}')}{b\,(1-\mathrm{tr}(\boldsymbol{\alpha}^{s})/b)^{2}}$	Relaxation.
RHS3	$-u^{s}_{x}\dfrac{\partial\alpha'_{xx}}{\partial x}$	Convection of conformation deviations by the steady-state x-velocity.
RHS4	$-u^{s}_{y}\dfrac{\partial\alpha'_{xx}}{\partial y}$	Convection of conformation deviations by the steady-state y-velocity.
RHS5	$-u'_{x}\dfrac{\partial\alpha^{s}_{xx}}{\partial x}$	Convection of the steady-state conformation by x-velocity deviations.
RHS6	$-u'_{y}\dfrac{\partial\alpha^{s}_{xx}}{\partial y}$	Convection of the steady-state conformation by y-velocity deviations.
RHS7	$2\alpha^{s}_{xx}\dfrac{\partial u'_{x}}{\partial x}$	Stretching caused by deviations in the extension rate.
RHS8	$2\alpha^{s}_{xy}\dfrac{\partial u'_{x}}{\partial y}$	Stretching caused by deviations in the shear rate.
RHS9	$2\alpha'_{xx}\dfrac{\partial u^{s}_{x}}{\partial x}$	Stretching caused by deviations in the extensional stress.
RHS10	$2\alpha'_{xy}\dfrac{\partial u^{s}_{x}}{\partial y}$	Stretching caused by deviations in the shear stress.

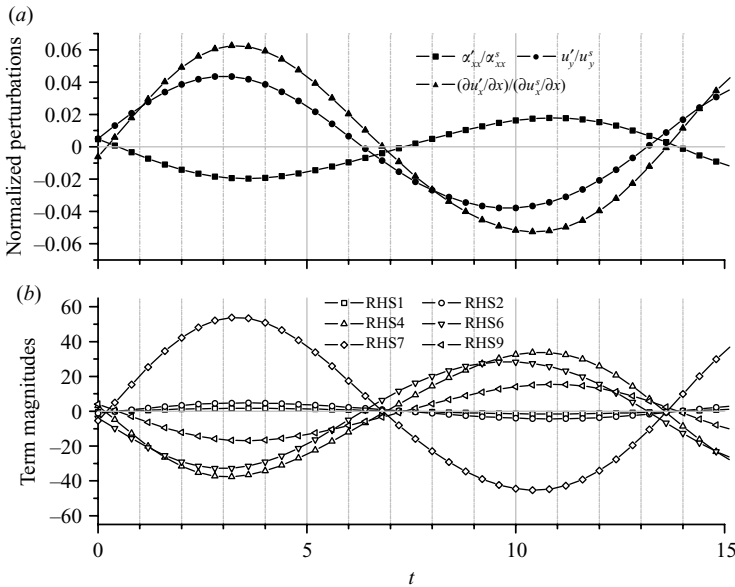TABLE 1. Terms on the right-hand side of (3.4).

FIGURE 13. Time-dependent oscillations at $(0,-0.05)$. (*a*) Perturbations of variables normalized by steady-state quantities; (*b*) magnitudes of terms on RHS of (3.4).

affect our analysis was seen. Correspondingly, deviations in polymer conformation, inflow velocity and extension rate, normalized by steady-state values, are plotted in figure 13(*a*).
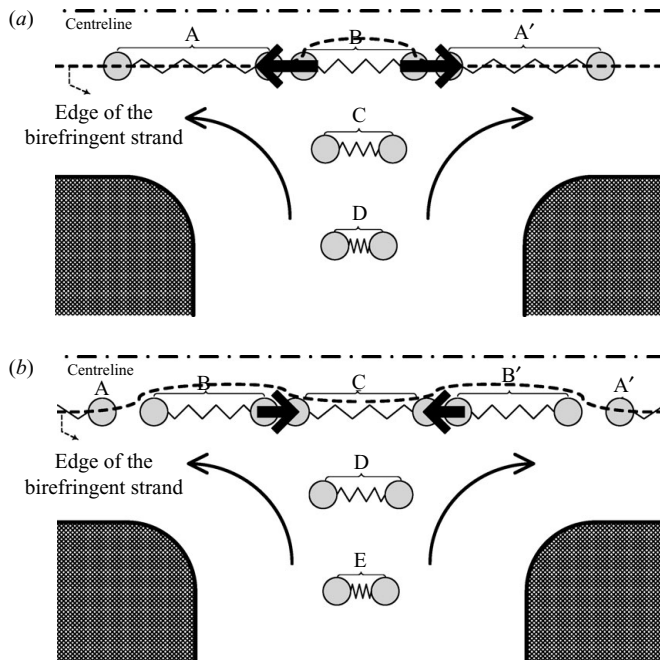
FIGURE 14. Schematic of instability mechanism (view of the lower half geometry). Thick arrows represent net forces exerted by polymer molecules (dumbbells) on the fluid. (*a*) Thinning process of the birefringent strand. (*b*) Re-thickening process of the birefringent strand.

Consistent with our earlier observations, deviations in the velocity field (u'_y and $\partial u'_x/\partial x$) and deviations in stress field (α'_{xx}) are opposite in sign for most of the time within the period. Among the terms plotted, RHS4, RHS6, RHS7 and RHS9 are much larger than the relaxation terms, RHS1 and RHS2, and dominate the dynamics. (Relaxation terms are large at the very inner regions of the birefringent strand and that is why oscillations in the stress field there are barely noticeable.) Moreover, RHS4, RHS6 and RHS9 are mostly in phase with α'_{xx}, and thus tend to enhance the deviations while RHS7 is out of phase with α'_{xx}, and hence damps the deviations. It is the joint effect of these competing destabilizing and stabilizing forces that gives the oscillatory behaviour of the system. Finally, notice that among the three destabilizing terms, RHS6 is the one that leads the phase and thus guides the instability.

Based on these observations from figure 13, a mechanism for the instability can be proposed, which is illustrated schematically in figure 14. At the beginning of the cycle ($t = 0$), u'_y is slightly above zero, indicating that the inflow speed is faster than that in the steady state. As a consequence, RHS6 becomes negative first, followed by RHS4 and RHS9. In particular, a faster incoming convective flow brings unstretched polymer molecules toward the stagnation point (corresponding to RHS6), as depicted in figure 14(*a*). These polymer chains have less time to be stretched and when they reach the edges of the birefringent strand (e.g. dumbbell B), they are less stretched compared with the steady state. As a result, fluid around dumbbell B has lower stress than at the steady state, corresponding to a thinning of the birefringent strand. Meanwhile, since dumbbell B contains smaller spring forces than its downstream neighbours A and A', the net forces (thick arrows) exerted by the polymer on the fluid point outward, generating jets downstream from the stagnation point. (In other

words, when the stress at the centre is lower, the net stress divergence points outward, which increases momentum in the downstream directions.) By continuity, more fluid has to be drawn toward the stagnation point and the initial deviation in u'_y is then enhanced. However, as the flow speeds up in the vicinity of the stagnation point, the extension rate also starts to increase. This effect (corresponding to RHS7) tends to stretch polymer molecules more and stabilize the deviations, as shown in figure 13. Eventually this effect will be able to overcome that of RHS6 as well as RHS4 and RHS9 and the stress near the stagnation point starts to increase after it passes the minimum at around $t = 3.5$, which causes a re-thickening of the birefringent strand figure 14(b). By a similar argument to that above, dumbbell C has higher spring forces than B and B′, the dumbbells which were passing near the centre when stress was at minimum, and the net polymer forces point inward, which starts to suppress the jets. Inflow velocity decreases as the birefringent strand thickens and this gives incoming polymer molecules more time to be stretched, and further thickens the birefringent strand. Eventually, α_{xx} will return to the steady-state value at around $t = 7.2$. However, since all the deviations are not synchronized, a negative deviation is found in u_y and an identical analysis with opposite signs can be made for the second half of the cycle.

Within this mechanism, a sharp edge of the birefringent strand, i.e. large magnitude of $\partial \alpha_{xx} / \partial y$ ($\sim O(10^4)$ in our simulations), is required so that a small u'_y can give a sufficiently large RHS6 to drive the instability. This is made possible by the kinematics of the flow near the stagnation point, where the incoming polymer molecules are strongly stretched within a short distance. Another similar effect is that stress derivatives are stretched in the outgoing direction and thus greatly weakened as fluid moves downstream; therefore, the instability is dominated by physics in the vicinity of the stagnation point. In the earlier mechanism for the so-called 'varicose instability', given by Harris & Rallison (1994), the importance of extensional stress and flow kinematics, especially the role of convection of incoming molecules, was also recognized. However, the picture described in their work is not the same as ours owing to the simplifications in their model. Their linear stability analysis ignores the x-dependence of the birefringent width whereas in our simulations, x-dependence of the stress field is closely related to the changes in velocity field. Besides, their analysis does not identify a restoring force for the deviations and the oscillatory behaviour could not be explained.

4. Conclusions

Using a DEVSS/SUPG formulation of the finite-element method, we are able to simulate viscoelastic stagnation-point flow and obtain steady-state and time-dependent solutions at high *Wi*. For *Wi* $\gg 1$, a clear birefringent strand is observed. The width of this birefringent strand increases with increasing *Wi* until *Wi* ≈ 40, after which it declines gradually. This also results in a non-monotonic trend in the modification of the velocity field.

At around *Wi* $= 65$, the steady-state solution loses stability and a periodic orbit becomes the attractor in phase space. Flow motion of the periodic orbit is characterized by time-dependent fluctuations, specifically, alternating positive (jet) and negative (wake) deviations from the steady-state velocity in the regions downstream of the stagnation point. A mechanism is proposed which, taking account of the interaction between velocity and stress fields, is able to explain the whole process of the oscillatory instability. Extensional stresses and their gradients, as well as the flow kinetics near the stagnation points, are identified as important factors in the mechanism. This mechanism is different from that of the 'hoop stress' instabilities,

which occur in viscometric flows with curved streamlines, and we expect that this mechanism could be extended to explain various instabilities occurring in viscoelastic flows with stagnation points.

REFERENCES

ARRATIA, P. E., THOMAS, C. C., DIARIO, J. & GOLLUB, J. P. 2006 Elastic instabilities of polymer solutions in cross-channel flow. *Phys. Rev. Lett.* **96**, 144502.

BAAIJENS, F. P. T. 1998 Mixed finite element methods for viscoelastic flow analysis: a review. *J. Non-Newtonian Fluid Mech.* **79**, 361–385.

BAAIJENS, F. P. T., SELEN, S. H. A., BAAIJENS, H. P. W., PETERS, G. W. M. & MEIJER, H. E. H. 1997 Viscoelastic flow past a confined cylinder of a low density polyethylene melt. *J. Non-Newtonian Fluid Mech.* **68**, 173–203.

BIRD, R. B., CURTIS, C. F., ARMSTRONG, R. C. & HASSAGER, O. 1987 *Dynamics of Polymeric Liquids*, 2nd edn, vol. 2. Wiley Interscience.

BISGAARD, C. 1983 Velocity fields around spheres and bubbles investigated by laser-Doppler anemometry. *J. Non-Newtonian Fluid Mech.* **12**, 283–302.

BISGAARD, C. & HASSAGER, O. 1982 An experimental investigation of velocity fields around spheres and bubbles moving in non-Newtonian fluids. *Rheol. Acta.* **21**, 537–539.

BROADBENT, J. M., POUNTNEY, D. C. & WALTERS, K. 1978 Experimental and theoretical aspects of the two-roll mill problem. *J. Non-Newtonian Fluid Mech.* **3**, 359–378.

BROOKS, A. N. & HUGHES, T. J. R. 1982 Streamline upwind/Petrov–Galerkin formulations for convection dominated flows with particular emphasis on the incompressible Navier–Stokes equations. *Comput. Math. Appl. Mech. Eng.* **32**, 199–259.

CHOW, A., KELLER, A., MÜLLER, A. J. & ODELL, J. A. 1988 Entanglements in polymer solutions under elongational flow: a combined study of chain stretching, flow velocimetry, and elongational viscosity. *Macromolecules* **21**, 250–256.

GRAHAM, M. D. 1998 Effect of axial flow on viscoelastic Taylor–Couette instability. *J. Fluid Mech.* **360**, 341–374.

GRAHAM, M. D. 2003 Interfacial hoop stress and instability of viscoelastic free surface flows. *Phys. Fluid* **15**, 1702–1710.

GROISMAN, A. & STEINBERG, V. 2000 Elastic turbulence in a polymer solution flow. *Nature* **405**, 53–55.

GROISMAN, A. & STEINBERG, V. 2001 Efficient mixing at low Reynolds numbers using polymer additives. *Nature* **410**, 905–908.

GROISMAN, A. & QUAKE, S. R. 2004 A microfluidic rectifier: anisotropic flow resistance at low Reynolds number. *Phys. Rev. Lett.* **92**, 094501.

GROISMAN, A., ENZELBERGER, M. & QUAKE, S. R. 2003 Microfluidic memory and control devices. *Science* **300**, 955–958.

GUCKENHEIMER, J. & HOLMES, P. 1983 *Nonlinear Oscillations, Dynamical Systems and Bifurcations of Vector Fields*. Springer.

HARLEN, O. G. 2002 The negative wake behind a sphere sedimenting through a viscoelastic fluid. *J. Non-Newtonian Fluid Mech.* **108**, 411–430.

HARLEN, O. G., RALLISON, J. M. & CHILCOTT, M. D. 1990 High-Deborah-number flows of dilute polymer solutions. *J. Non-Newtonian Fluid Mech.* **34**, 319–349.

HARRIS, O. J. & RALLISON, J. M. 1993 Start-up of a strongly extensional flow of a dilute polymer solution. *J. Non-Newtonian Fluid Mech.* **50**, 89–124.

HARRIS, O. J. & RALLISON, J. M. 1994 Instabilities of a stagnation point flow of a dilute polymer solution. *J. Non-Newtonian Fluid Mech.* **55**, 59–90.

HASSAGER, O. 1979 Negative wake behind bubbles in non-Newtonian liquids. *Nature* **279**, 402–403.

JOO, Y. L. & SHAQFEH, E. S. G. 1994 Observations of purely elastic instabilities in Taylor–Dean flow of a Boger fluid. *J. Fluid Mech.* **262**, 27–73.

LARSON, R. G. 1992 Instabilities in viscoelastic flows. *Rheol. Acta.* **31**, 213–263.

LARSON, R. G., MULLER, S. J. & SHAQFEH, E. S. G. 1990 A purely elastic instability in Taylor–Couette flow. *J. Fluid Mech.* **218**, 573–600.

MCKINLEY, G. H., ARMSTRONG, R. C. & BROWN, R. A. 1993 The wake instability in viscoelastic flow past confined circular cylinders. *Phil. Trans. R. Soc. Lond.* A **344**, 265–304.

MAGDA, J. J. & LARSON, R. G. 1988 A transition occurring in ideal elastic liquids during shear flow. *J. Non-Newtonian Fluid Mech.* **30**, 1–19.

MÜLLER, A. J., ODELL, J. A. & KELLER, A. 1988 Elongational flow and rheology of monodisperse polymers in solution. *J. Non-Newtonian Fluid Mech.* **30**, 99–118.

MULLER, S. J., SHAQFEH, E. S. G. & LARSON, R. G. 1989 A purely elastic transition in Taylor–Couette flow. *Rheol. Acta.* **28**, 499–503.

NG, R. C. Y. & LEAL, L. G. 1993 Concentration effects on birefringence and flow modification of semidilute polymer solutions in extensional flows. *J. Rheol.* **37**, 443–468.

PAKDEL, P. & MCKINLEY, G. H. 1996 Elastic instability and curved streamlines. *Phys. Rev. Lett.* **77**, 2459–2462.

POOLE, R. J., ALVES, M. A. & OLIVEIRA, P. J. 2007 Purely elastic flow asymmetries. *Phys. Rev. Lett.* **99**, 164503.

REMMELGAS, J., SINGH, P. & LEAL, L. G. 1999 Computational studies of nonlinear elastic dumbbell models of Boger fluids in a cross-slot flow. *J. Non-Newtonian Fluid Mech.* **88**, 31–61.

RENARDY, M. 2006 A comment on smoothness of viscoelastic stresses. *J. Non-Newtonian Fluid Mech.* **138**, 204–205.

SHAQFEH, E. S. G. 1996 Purely elastic instabilities in viscometric flow. *Annu. Rev. Fluid. Mech.* **28**, 129–185.

SPIEGELBERG, S. H. & MCKINLEY, G. H. 1996 Stress relaxation and elastic decohesion of viscoelastic polymer solutions in extensional flow. *J. Non-Newtonian Fluid Mech.* **67**, 49–76.

SQUIRES, T. M. & QUAKE, S. R. 2005 Microfluidics: fluid physics at nanoliter scale. *Rev. Mod. Phys.* **77**, 977–1026.

THOMASES, B. & SHELLEY, M. 2007 Emergence of singular structures in Oldroyd-B fluids. *Phys. Fluid* **19**, 103103.